HIL implementation of an islanding detection and an automatic mode switching for droop-based microgrid

Shreeram V. Kulkarni* and
Dattatraya N. Gaonkar

Department of Electrical and Electronics Engineering,
National Institute of Technology Karnataka,
Surathkal Mangalore-575025, Karnataka, India
Email: vshreeramk@gmail.com
Email: dngaonkar@gmail.com
*Corresponding author

Abstract: This paper presents the control schemes and performance study of parallel connected inverter based distributed generation sources (DGs) in microgrid for grid-connected and stand-alone modes of operation. This standalone mode of operation of inverter based DG system is mainly based on droop control scheme with the virtual complex impedance in the outer voltage loop. The microgrid load power is proportionally shared by the DGs according to their power ratings which features a good reliability and efficiency. Both the modes are switched automatically based on the Phase Locked Loop (PLL) phase error $\sin(\gamma - \theta)$. This phase error is used to detect the islanding during disturbances in the system and also helps in seamless transfer between the modes. The PLL phase error response, islanding detection and mode switching are presented for various fault conditions. The hardware-in-the-loop (HIL) based platform is used to evaluate the performance of the microgrid in both the modes with islanding detection and automatic mode switching operation.

Keywords: microgrid; inverter parallel operation; droop control; phase locked loop; islanding detection; automatic mode switching; hardware in the loop.

Reference to this paper should be made as follows: Kulkarni, S.V. and Gaonkar, D.N. (2022) 'HIL implementation of an islanding detection and an automatic mode switching for droop-based microgrid', *Int. J. Power Electronics*, Vol. 15, No. 1, pp.37–54.

Biographical notes: Shreeram V. Kulkarni received his MTech in Electrical Power Systems from Shri Dharmasthala Manjunatheshwara College of Engineering and Technology, Dhavalagiri Dharwad., India in 2016. He is pursuing his PhD in Power Systems from National Institute of Technology Karnataka, Surathkal, India.

Dattatraya N. Gaonkar received his MTech in Power and Energy Systems from National Institute of Technology Karnataka, Surathkal, India in 2003. He obtained his PhD in Power Systems in 2008 from Indian Institute of Technology (IIT), Roorkee, India. He was a Visiting Scholar at the University of Saskatchewan Canada. He also visited the Center for Future Energy Systems (CFES) at Rensselaer Polytechnic Institute (RPI), Troy New York and Energy Reliability and Security Laboratory at Michigan State University (MSU) at East Lansing, USA and Energy Management and Microgrid Laboratory at NUS Singapore for research interaction. He has edited and written a chapter in the book titled *Distributed Generation*, which is published by INTECH Publication

Copyright © 2022 Inderscience Enterprises Ltd.

Austria. He is a senior member of IEEE and Fellow of IE (India), life member of ISTE and SSI. His main research interests are in the area of power system operation and control, distributed generation systems and power electronics. Presently, He is a faculty member in the Department of Electrical and Electronics Engineering NITK Surathkal.

1 Introduction

The electrical power system network is becoming more complex due to the recent trends in growing interconnections of small distributed generations (DGs). The controlling of DGs in the power distribution network is the most important one (Rocabert et al., 2012). There are several DGs mainly categorised into non-renewable and renewable resources, such as photovoltaic systems, wind farms, micro-turbine, fuel cells, geothermal, micro-hydro, biomass, tides and ocean waves. Among these micro-sources photovoltaic and wind plants are prominent sources suitable for integration through the power electronic converters. These DGs are potentially connected to any point in the power distribution network and are more feasible to integrate in the microgrid (Dragicevic et al., 2017). The microgrid concept is considered as a small-scale grid in the power system network, normally operates in both grid-connected (GC) mode and stand-alone (SA) mode. The control and operation of the DG sources in the power distribution network will make the overall system performance flexible and efficient in terms of potential benefits (Luna et al., 2015). Microgrid sources need to be controlled to provide nearly constant voltage and constant frequency operation when operated in SA mode and provide constant power injection in GC mode of operation. There are several power electronic topologies available such as DC-DC, AC-AC, DC-AC, AC-DC-AC converters, among these the AC-DC-AC topology considering back to back converter are preferred (Pouresmaeil et al., 2013; Bei, 2017). A well defined control strategy has to be implemented to ensure the proper transition between the GC mode and the SA mode of operation. Islanding detection is not an easy subject, also circuit breaker (CB) is not the only candidate to produce an islanding. There are several CBs in the networks to initiate an islanding (Redfern et al., 1993) at any time. The de centralised local measurement based droop control schemes are becoming important for islanding operation of microgrid (Bei, 2017; Wang et al., 2012; Guerrero et al., 2005).

The detailed microgrid system modelling with small signal stability analysis is presented in Pogaku et al. (2007) and Sun et al. (2017). The droop control technique is used for SA mode of operation for parallel connected inverter based DGs. The droop control technique is feasible due to their locally measured information and there is no loss of information due to the communication means (Gaonkar et al., 2010; Ketabi et al., 2017; Dou et al., 2017). In GC operation mode constant current control with phase locked loop (PLL) generator are incorporated in the control scheme (Bifaretti et al., 2015; Dong et al., 2014) frequency and voltage are maintained by the grid itself. Generally, PLL is used to track the frequency and phase angle of the grid for synchronisation and resynchronisation. The PLL is responsible for smooth transition between the GC mode and SA operation mode. The grid failure detection for wind turbine with linear balanced load of 11 kW is presented in Teodorescu et al. (2004). The conventional droop control technique will rely on the output impedance characteristics of the network. Due to this

the virtual complex impedance scheme is accomplished in the voltage controller loop Wang et al. (2015). The microgrid system model considered for the study is shown in Section 2, Figure 1. In this paper the droop control with virtual impedance scheme and standard current control scheme are incorporated for SA and GC mode of operation for parallel inverter-based DGs of different power ratings (10 kW and 5 kW). To validate the control scheme performance the Typhoon hardware-in-the-loop is used. The GC control scheme with PLL is presented in Section 3.1, Figure 3. The SA control scheme is presented in Section 3.2, Figure 4.

2 The microgrid system

The microgrid system model considered for the study is shown in Figure1. The parallel inverter-based DGs are connected to 230 volts 50 Hz grid at the point of common coupling (PCC). The system model consists of the following components: constant DC voltage source with breaking chopper, two three phase voltage source inverters (VSIs), LCL filter, distribution lines, parallel RLC load, circuit breaker (CB) and the grid. The test microgrid system parameters are given in Table 1. The microgrid system model also consists of a mode switch block, it is responsible for switching the respective modes (grid-connected to stand-alone) depending on the phase error ($\sin(\gamma - \theta)$). The synchronisation and re-synchronisation is done by the PLL as explained in Section 4.

Table 1 Test microgrid system parameters

Parameter	*Value*	*Parameter*	*Value*
R_s	0.01 Ω	k_{pv}	0.0263
C_{DC}	8e–4 F	k_{iv}	2.893
L_{inv}	5.082e–3 H	k_{pi}	13
R_{inv}	0.01 Ω	k_{ii}	1,430
C_f	2.104	X_{gl}	1.8e–3 H
R_f	1 Ω	R_{gl}	1 Ω
L_g	2.541e–3 H	ω_n	314.2 radians
R_g	0.5 Ω	V_{dn}	400 Volts
m_{p1}	2.5e–4	n_{q1}	1.33e–3
m_{p2}	5e–4	n_{q2}	2.66e–3
R_v	–1.2e–3 Ω	L_v	0.55e–3 H
$\Delta\theta$	0.3	f	50 Hz
X_l	1e–3 H	R_{load1}	11.25 Ω
R_l	0.8 Ω	R_{load}	4.5 Ω per phase
C_{load}	1.01e–4 F per phase	L_{load}	0.1 H per phase
F	0.5	ω_c	60 radians

Figure 1 The microgrid system model (see online version for colours)

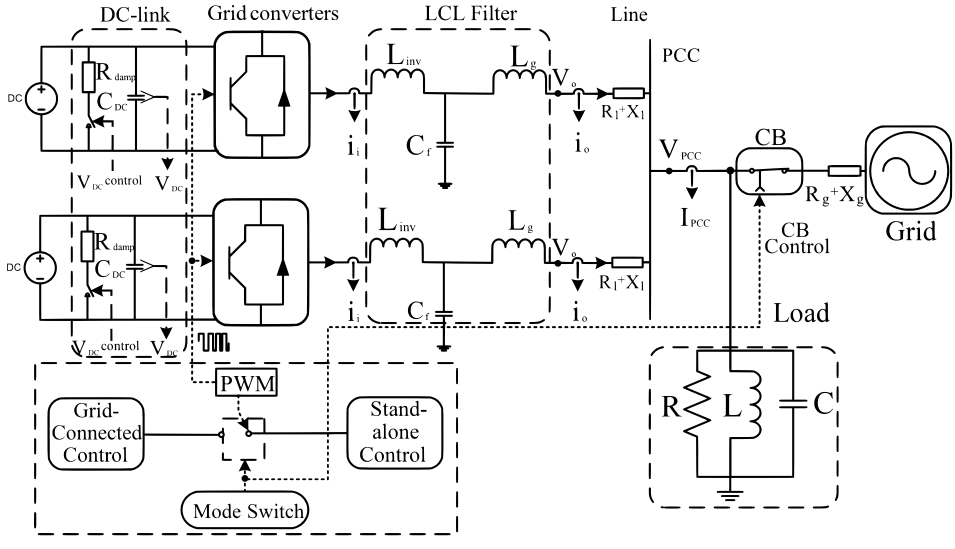

2.1 LCL filter and parallel RLC load

The LCL filter design and parallel RLC load modelling for inverter-based DGs is depicted in this section. The base impedance and base capacitance of the microgrid system is given by equation (1) (Reznik et al., 2014).

$$Z_{base} = \frac{V_{ph}^2}{P}; \qquad C_{base} = \frac{1}{\omega_n * Z_{base}} \tag{1}$$

where Z_{base} is base impedance and C_{base} is base capacitance, V_{ph} is the phase voltage, P is the rated active power and ω_n is the nominal angular frequency. The value of the filter capacitor is selected based on base capacitance of the microgrid system, and is given in equation (2).

$$C_f = \frac{C_{base}}{2} \tag{2}$$

The filter inductance is designed on the basis of maximum current ripple of the inverters. Here we considered maximum current ripple of 10% and is given by equation (3).

$$\Delta I_{\max} = 0.1 * I_{\max} \tag{3}$$

where $I_{\max}$ is given in equation (4)

$$I_{\max} = \frac{P_{rated} * \sqrt{2}}{3 * V_{ph}} \tag{4}$$

The filter inductances L_{inv} and L_g are given in equation (5).

$$L_{inv} = \frac{V_{DC}}{6 * f_{sw} * \Delta I_{\max}}; \qquad L_g = 0.5 * L_{inv} \tag{5}$$

where L_{inv} is inverter side filter inductance, L_g is grid side filter inductance, f_{sw} is inverter switching frequency and VDC is DC-link voltage. The parallel RLC load is considered as a general structure of the local load. According to the IEEE 1547.1 test setup a parallel RLC load is connected in between the inverter-based DGs and the grid (IEEE, 2009; Basso, 2014). The modelling of the parallel RLC load includes: The active power P_{load} in kW, reactive power Q_{load} in kVAr, resonance frequency f_o in Hz and quality factor Q_f. The modelling equations are given in equations (6) and (7).

$$P_{load} = \frac{V_{PCC}^2}{R}; \qquad Q_{load} = V_{PCC}^2 \left(\frac{1}{\omega L} - \omega c \right) \tag{6}$$

$$f_o = \frac{1}{2\pi\sqrt{LC}}; \qquad Q_f = R\sqrt{\frac{C}{L}} \tag{7}$$

where the $V_{PCC} = V_{grid}$ in GC operation mode and $V_{PCC} = V_{DG}$ in SA operation mode. And L is load inductance in Henry, C is load capacitance in Farad and ω is angular frequency of microgrid system. The bode plots of LCL filter and parallel RLC load is shown in Figure 2. A peak response is seen at 11.7 dB, –15.9 dB magnitude and the high frequency is around 1.24e^3 depicts the good system dynamics.

Figure 2 Bode plots for LCL filter and parallel RLC load (see online version for colours)

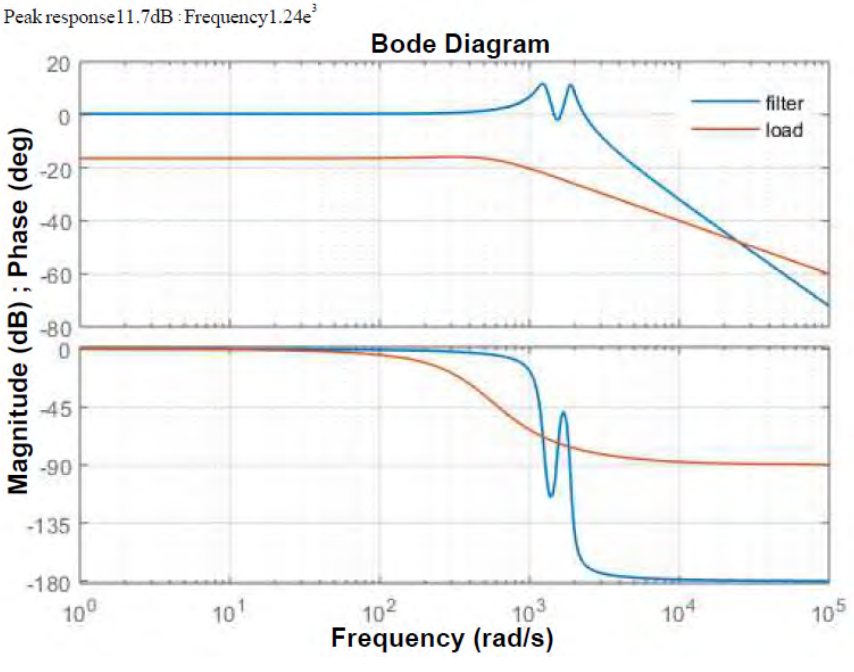

3 Control schemes for grid-connected and islanding operation modes

3.1 Grid-connected mode

In GC operation mode the power generated by the inverter-based DGs is transferred to the microgrid system load and excess generated power is being transferred to the grid. If microgrid system load demand is more than the power generated by DGs, then the grid takes up the excess load. In GC mode of operation it is easy to conclude that the total microgrid system load demand is being supplied by both the inverter-based DGs and the grid and is shown in equation (8).

$$V_{PCC} = V_G$$
$$P_{load} = P_{DG} + P_{grid}; \qquad Q_{load} = Q_{DG} + Q_{grid} \tag{8}$$

where V_{PCC} is voltage at point of common coupling, V_{grid} is grid voltage, P_{DG}, P_{grid}, P_{load} and Q_{DG}, Q_{grid}, Q_{load} are inverter, grid, load active powers in kW and reactive powers in kVAr respectively. If the DGs are generating excess power which is more than the required microgrid system load demand then the excess will be exported to the grid and is shown in equation (9).

$$P_{DG} = P_{load} + P_{grid}; \qquad Q_{DG} = Q_{load} + Q_{grid} \tag{9}$$

The GC control scheme is shown in Figure 3.

Figure 3 (a) Control scheme for grid connected mode (b) Phase locked loop (see online version for colours)

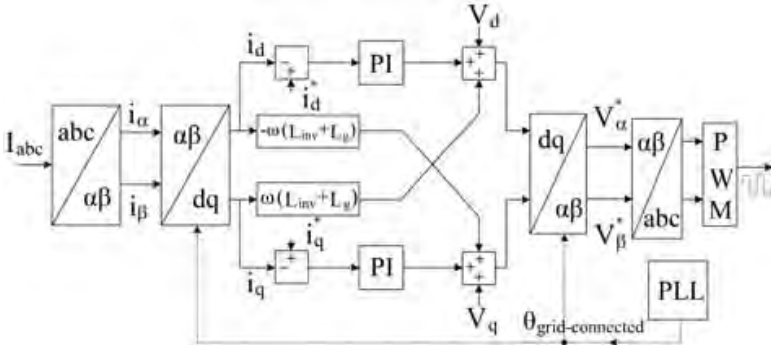

(a)

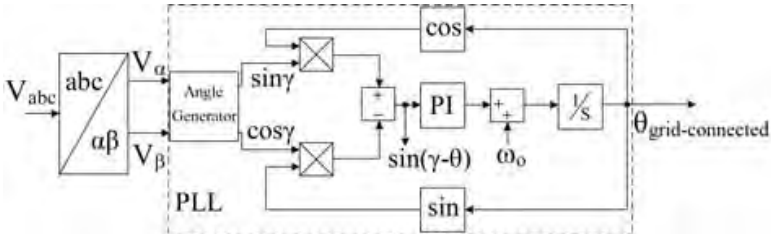

(b)

The grid currents and voltages are being regulated by standard PI controllers in inner and outer control loops respectively. The q-axis reference current is set to zero to achieve the zero phase angle difference between the voltage and current. A decoupling of cross-coupling is implemented in outer control loop to compensate the coupling due to the LCL filters in the microgrid system model. The control signals for the inverter-based DGs are being generated by standard PWM technique. The PLL for GC mode of operation is explained in the next subsection.

3.2 Stand-alone mode

In SA operation mode there is no impact of the grid on the inverter-based DGs. The PCC voltages are equal to the inverter front-end voltages. And all the critical loads are supplied by the DGs itself while maintaining the voltage and frequency in the prescribed limits. The voltage, active power and reactive power equations are shown in equation (10).

$$\begin{aligned} V_{PCC} &= V_{DG} \\ P_{load} &= P_{DG}; Q_{load} = Q_{DG} \end{aligned} \tag{10}$$

If connected microgrid system load is greater than DGs generated power then the system will go into the unstable region, is given by equation (11).

$$P_{load} > P_{DG}; Q_{load} > Q_{DG} \tag{11}$$

In this scenario proper control technique has to be implemented to ensure the stable SA operation mode. The load shifting, load cutting and hike in the DGs generated powers are the some general techniques to be adopted Lin et al (2017). The active power versus frequency and reactive power versus voltage droop slopes (Ketabi et al., 2017; Guerrero et al., 2004) for both the DGs are shown in Figure 4.

The droop coefficients for parallel inverter-based DGs having equal power ratings to share the load proportionally are given in equation (12).

$$m_{p1} = m_{p2}; n_{q1} = n_{q2} \tag{12}$$

In this system the DG1 has maximum power rating 10 kVA, the droop slopes of active power and frequency curve is higher than that of other DG2 having a power rating of 5 kVA and droop coefficients are given by equation (13).

$$m_{p1} = 2 * m_{p2}; n_{q1} = 2 * n_{q2} \tag{13}$$

The SA mode control technique for inverter-based DGs is shown in Figure 4. The droop control is implemented in the power loop for the inverter-based DGs. Frequency and voltages are regulated in accordance with the active power and reactive power variations respectively. The frequency and voltage droops are given by equation (14).

$$\begin{aligned} \omega^* &= \omega_n - m_p P \\ V^* &= V_{dn} - n_p Q \end{aligned} \tag{14}$$

where ω^* and V^* are frequency and voltage references, ω_n and V_{dn} are the nominal microgrid system frequency and voltage, P and Q are the calculated real and reactive power outputs of the DGs, P_{max} and Q_{max} are the maximum real and reactive powers of the DGs. The droop slopes m_p and n_q are depicted in equation (15).

$$m_p = \frac{\omega_{max} - \omega_{min}}{P_{max}}$$
$$n_q = \frac{V_{max} - V_{min}}{Q_{max}} \tag{15}$$

Figure 4 (a) P-f droop right: Q-V droop (b) Control scheme for stand alone mode (see online version for colours)

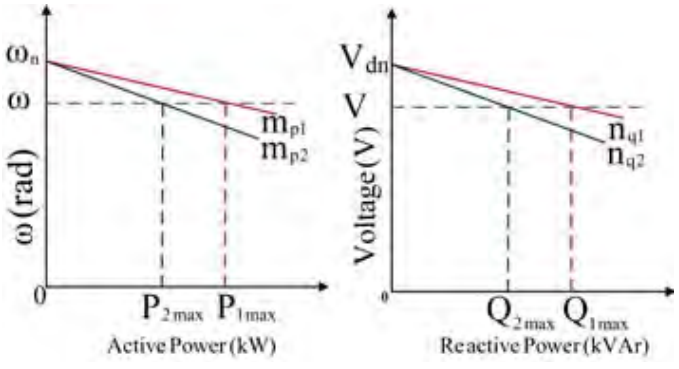

(a)

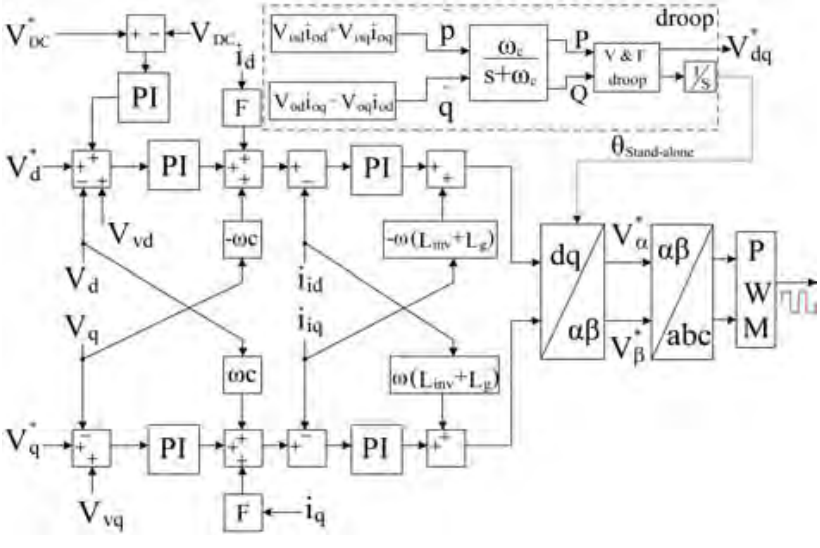

(b)

The equations for virtual complex impedance included in the voltage control loop are given by equations (16) and (17).

$$V_{vd} = i_{od} * R_v - \frac{di_{oq}}{dt} * L_v \tag{16}$$

$$V_{vq} = i_{oq} * R_v - \frac{di_{od}}{dt} * L_v \tag{17}$$

where V_{vd} and V_{vq} are virtual *d*-*q*-axis voltage references and i_{od} and i_{oq} are the inverter *d*-*q*-axis output currents. R_v and L_v are the components of virtual complex impedance. The voltage and current controller for inverters is employed with standard PI controller, feed-forward gain, feed-back gain, proportional gain, and integral gain. The virtual complex impedance is implemented in voltage control loop for the inverter-based DGs to improve the dynamics of the system and to reduce the circulating currents (Bei, 2017; Wang et al., 2015; Guerrero et al., 2004). The output DC-link voltage control is activated only when the reference voltage is more than the DC-link voltage. The principle of this control is to maintain the reference voltage to its standard. If the DC-link voltage is higher than the reference voltage the chopper control will be activated to dissipate the extra energy. The dissipation of excess energy through the damping resistor is done by activating the damping chopper control, there by maintaining the DC-link voltage to its reference (Teodorescu et al., 2004). The inverter control is implemented in d-axis frame and q-axis reference is made zero. A decoupling of the cross-coupling is implemented in the control structure due to LCL filters in the system. The PWM technique is used to generate the control signals for the inverter-based DGs (Bei, 2017; Dou et al., 2017; Lin et al., 2017).

4 PLL and islanding detection

The inverter-based DGs are synchronised to the grid by the PLL. In Teodorescu et al. (2004) a PLL is proposed which is capable of grid failure detection. The sinusoidal phase angle difference between the grid and the DG is formulated as given below.

$$V_{abc} = [T]V_{\alpha\beta} \tag{18}$$

where V_{abc} are the measured three phase voltages of the grid and T is the Clark transformation matrix, given as $[T] = 0.8165 * \begin{bmatrix} 1 & 0 \\ -.0.5 & 0.866 \\ -0.5 & -0.866 \end{bmatrix}$. And $V_{\alpha\beta}$ are the Clark transformed grid voltages and are given by equations (19) and (20).

$$V_\alpha = V_a - 0.5 * V_b - 0.5 * V_c \tag{19}$$

$$V_\beta = 0.866 * V_b - 0.866 * V_c \tag{20}$$

The phase angle between these two grid voltage components can be calculated as equations (21) and (22).

$$\sin(\gamma) = \frac{V_\alpha}{\sqrt{V_\alpha^2 + V_\beta^2}} \tag{21}$$

$$\cos(\gamma) = \frac{V_\beta}{\sqrt{V_\alpha^2 + V_\beta^2}} \tag{22}$$

With the help of sinγ and cosγ we can calculate the DGs phase angle in the grid-connected mode of operation $\theta_{grid\text{-}connected}$. Then the phase locking between the DGs and the grid will be decided.

The phase difference between sinγ and cosγ quantities and the DGs phase angle is the the PLL phase error signal sin($\gamma - \theta$) as shown in Figure 5. The phase error signal sin($\gamma - \theta$) is used to detect the islanding and also used to switch the corresponding modes of operation. During the grid connect-mode due to faults/disturbances in one or more lines, the PLL generated phase error will exceed the threshold value. And this error exceeding the set threshold is considered as the grid failure and consequently the SA control mode is switched. The PLL control signals are shown in Figure 5. The PLL used in this paper satisfactorily works for a droop based parallel inverter configuration, as opposed to single inverter in Teodorescu et al. (2004).

Figure 5 PLL control signals for islanding detection (see online version for colours)

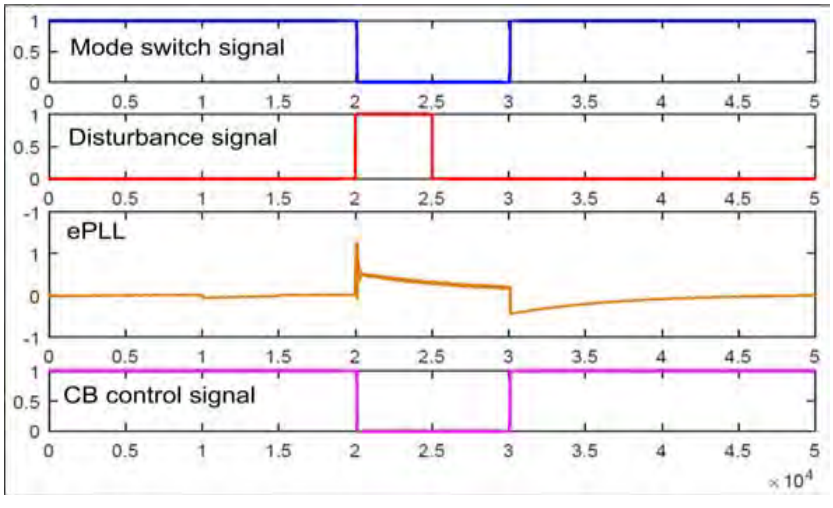

5 Result and discussion

The GC and SA control schemes for microgrid system model in Figure 1 is tested experimentally on the real-time Hardware in the loop (HIL) platform T. HIL (2017) and is shown in Figure 6. The mode switch block switches the GC operation mode and SA operation mode depending on required set points 1 (grid-connected mode) or 0 (stand-alone mode) received from the PLL. A fault is created at 2.0 sec and is sustained up to 2.5 sec. The responses are plotted for three cases as follows:

1 GC: Grid-connected mode of operation.

2 SA: Stand-alone mode of operation.

3 GC-SA-GC: Transition between grid-connected mode and stand-alone mode.

Figure 6 Hardware-in-the-loop experimental setup (see online version for colours)

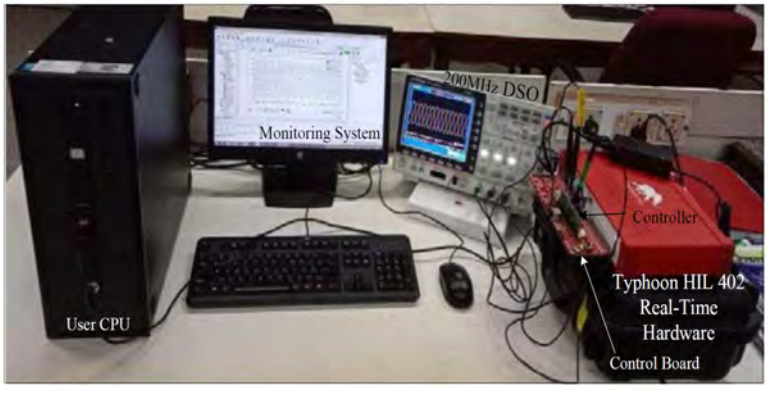

Case 1 GC: grid-connected mod

Figure 7 shows the grid-connected mode of operation, where mode switch block receives set point signal 1 from PLL thus the GC operation mode will be switched. Three phase load voltages and currents are shown in Figure 7(a) and 7(b). We can see the load currents variations in terms of load changes as: 0.0 sec–0.5 sec and 0.5 sec–1.5 sec.

In Figure 7(c) PLL γ, θ, $\sin(\gamma - \theta)$ and frequency at point of common coupling are shown. The zero crossing is not affected and PLL maximum phase error response reaches a value of 0.04 and then settles to 0.02. PCC frequency will operate at 50 Hz. Figure 7(d) shows active powers P_{load}, P_{grid}, P_{DG1} and P_{DG2}. At no load the generated power is being exported to the grid and when the load switches at 0.5 sec the load demand is supplied by the DGs and the grid, summarised in Table 2.

Figure 7 Grid-connected operation mode (a) load voltages in Volts (b) load currents in Amps (c) PLL (γ, θ, $\sin(\gamma - \theta)$) and PCC frequency (d) active power in kW (see online version for colours)

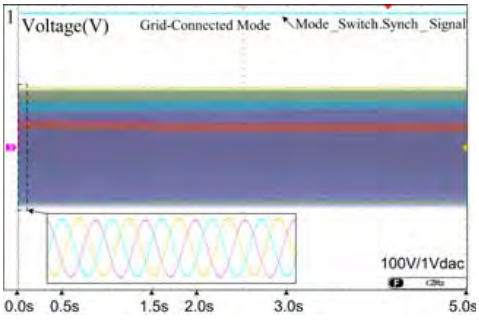

(a)

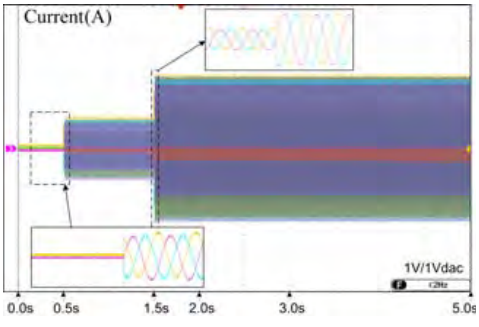

(b)

Figure 7 Grid-connected operation mode (a) load voltages in Volts (b) load currents in Amps (c) PLL (γ, θ, sin($\gamma - \theta$)) and PCC frequency (d) active power in kW (continued) (see online version for colours)

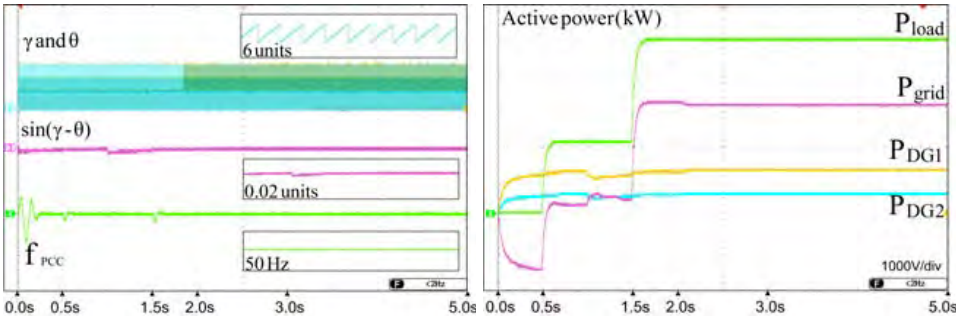

(c) (d)

Table 2 GC mode

Power	*0.0–0.5 sec*		*0.5–1.5 sec*		*1.5–5.0 sec*	
	P(kW)	*Q (kVAr)*	*P(kW)*	*Q (kVAr)*	*P(kW)*	*Q (kVAr)*
Load	-	-	8.0	0.2	20.0	0.07
Grid	–6.0	–0.75	1.0	–0.02	12.5	–0.3
DG1	4.0	0.5	4.6	0.15	5.0	0.25
DG2	2.0	0.25	2.3	0.07	2.5	0.12

Case 2 SA: stand-alone mode

The results for stand-alone operation mode are shown in Figure 8. The mode switch block receives set point signal 0 from PLL sin($\gamma - \theta$), the operation mode will be switched to the stand-alone mode. Three phase load voltages and currents are shown in Figure 8(a) and Figure 8(b).We can see the load voltages and currents variations in terms of load changes as: 0.0 sec–0.5 sec and 0.5 sec–1.5.

Figure 8 Stand-alone operation mode (a) load voltages in Volts (b) load currents in Amps (c) PLL (γ, θ, sin($\gamma - \theta$)) and PCC frequency (d) active power in kW (see online version for colours)

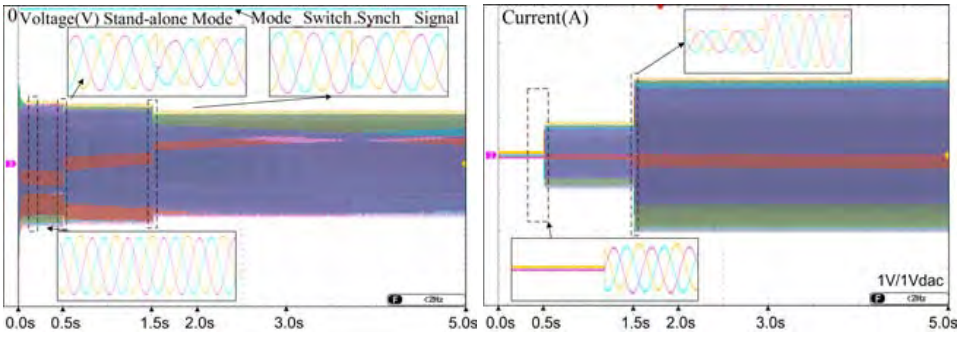

(a) (b)

Figure 8 Stand-alone operation mode (a) load voltages in Volts (b) load currents in Amps (c) PLL (γ, θ, sin($\gamma - \theta$)) and PCC frequency (d) active power in kW (continued) (see online version for colours)

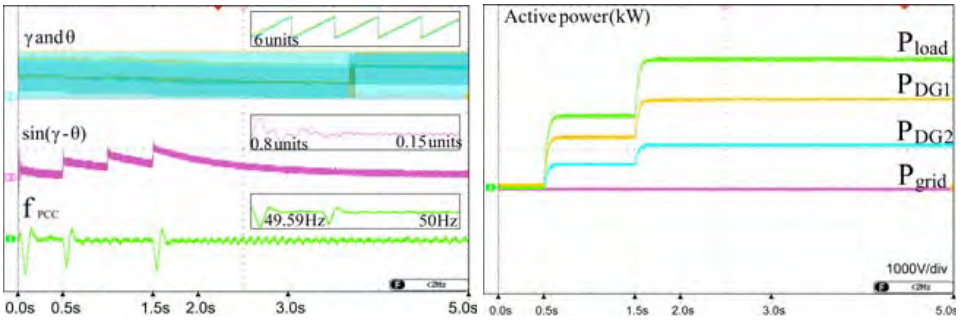

(c) (d)

Table 3 SA mode

Power	*0.0–0.5 sec*		*0.5–1.5 sec*		*1.5–5.0 sec*	
	P(kW)	*Q (kVAr)*	*P(kW)*	*Q (kVAr)*	*P(kW)*	*Q (kVAr)*
Load	-	-	8.0	-	20.0	-
Grid	-	-	-	-	-	-
DG1	-	-	5.2	0.16	9.5	0.3
DG2	-	-	2.6	0.07	5.5	0.12

In Figure 8(c) PLL γ, θ, sin($\gamma - \theta$) and frequency at point of common coupling are shown. There is no impact of the grid on the DGs, we can see small variations in PLL γ, θ but the zero crossing is not effected and and PLL maximum phase error sin($\gamma - \theta$) response is seen to be 0.8 and then settles to 0.15. Maximum 50.21 Hz and minimum 49.59 Hz variations are seen in the PCC frequency. The variations are in standard limits and 1.5 sec onwards it continues to operate at 50Hz. In Figure 8(d) active powers P_{load}, P_{grid}, P_{DG1} and P_{DG2}. As there is no grid, power generated by DGs is being supplied to the load demand in SA mode, shown in Table 3.

Case3 GC-SA-GC: transition between grid-connected and stand-alone mode

In Figure 9 the set point 1 is for GC mode and 0 for SA mode. Three phase load voltages and currents are shown in Figure 9(a) and Figure 9(b). Grid disturbance is introduced at 2.0 sec and 3.004 sec we can see the voltage and current spikes due to the mode switching operation. The mode will switch automatically to the respective operation mode. In Figure 9(c) PLL γ, θ, sin($\gamma - \theta$) and frequency at point of common coupling are shown.

Figure 9 GC-SA-GC operation mode (a) load voltages in Volts (b) load currents in Amps (c) PLL (γ, θ, sin($\gamma - \theta$))and PCC frequency (d) active power versus frequency plot (see online version for colours)

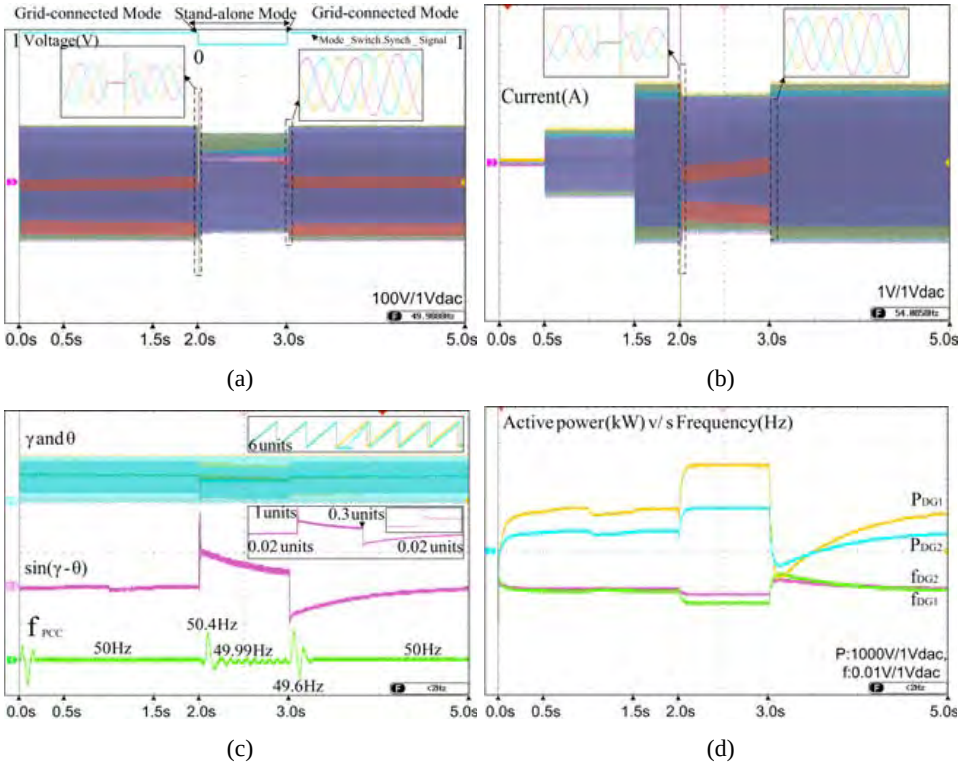

The γ, θ can be seen during the switching, and the signal sin($\gamma - \theta$) is used to detect islanding and automatic mode switching. Initially the system is operating in the GC mode, when the disturbance occurs the sin($\gamma - \theta$) will exceed the threshold value and within 10.4 ms the PLL will detect an islanding and switches to SA operation mode. The fault is introduced at 2.0 sec to 2.5 sec but the system will continue in the SA operation mode up to 3.004 sec after fault clearance.

Table 4 Test results for transition between GC-SA-GC modes

Power	*0.0–0.5 sec*		*0.5–1.5 sec*		*1.5–5.0 sec*		*1.5–5.0 sec*		*1.5–5.0 sec*	
	P (kW)	*Q (kVAr)*	*P (kW)*	*Q (kVAr)*	*P (kW)*	*Q (kVAr)*	*P (kW)*	*Q (kVAr)*	*P (kW)*	*Q (kVAr)*
Load	-	-	8.0	0.2	20.0	0.7	15.0	-	20.0	0.7
Grid	–6.0	–0.75	1.0	–0.02	12.5	–0.3	-	-	12.5	–0.3
DG1	4.0	0.5	4.6	0.15	5.0	0.25	9.5	0.3	5.0	0.25
DG2	2.0	0.25	2.3	0.07	2.5	0.12	5.3	0.12	2.5	0.12

Table 5 PLL phase error responses (see online version for colours)

Nature of faults	*PLL phase error sin(γ – θ)*	*Detection by PLL (m sec)*	*Nature of faults*	*PLL phase error sin(γ – θ)*	*Detection by PLL (m sec)*
A-GND		15.2	A-B-GND		3.6
B-GND		11.9	A-C-GND		7
C-GND		8.5	B-C-GND		10.3
A-B		3.6	A-B-C		10.4
A-C		6.9	A-B-C-GND		10.4
B-C		10.2			

Note:

Figure 10 GC-SA-GC operation mode, (a) active power in kW (b) reactive power in kVAr (see online version for colours)

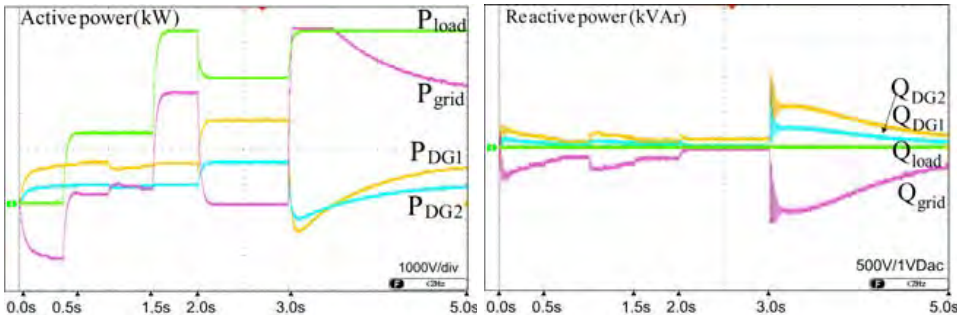

(a) (b)

At 3.004 sec the grid voltage settles down to a normal value and mode switch block switches the operation mode to GC operation mode. We can clearly see the variations of the PCC frequency (50.4Hz to 49.6Hz) during GC and SA mode switching. In Figure 9(d) the responses of active power versus frequency of both the DGs are shown. The droop controlled inverters will share the load proportionally depending on their power ratings. In Figure 10(a) and Figure 10(b) shows active powers P_{load}, P_{grid}, P_{DG1} and P_{DG2} and reactive powers Q_{load}, Q_{grid}, Q_{DG1} and Q_{DG2}. At no load the generated power is being exported to the grid and when the load switches at 0.5 sec the load demand is supplied by the DGs and the grid. At 2.0104 sec mode will switch to SA mode and power generated by DGs is being supplied to load demand. Again the mode will switch to GC mode at 3.004 sec after the fault clearing. The power exchange by the DGs, grid and the load are summarised in the Table 4 and Table 5 shows the PLL phase error responses for all type of faults in the system, the behaviour of responses with detection time by the PLL is also listed.

6 Conclusions

This paper presents the islanding detection and automatic mode switching of microgrid with parallel connected inverter-based DGs. By the experimental results, it can be concluded that, the control schemes for grid-connected and stand-alone operation modes exhibited a good performance for parallel connected inverter-based DGs in the microgrid. The implementation of the control schemes in the real-time hardware in the loop were examined and verified. The control scheme for stand-alone operation mode was executed with both droop control and virtual impedance loop and the same had been tested for two different power rating DGs. The test results shows that, the control schemes for decentralised DGs had a better performance in terms of power sharing in the multi DG environment. The control scheme for grid-connected operation mode was implemented with standard current controller including PLL. An islanding detection and automatic mode switching was done by the PLL phase error measurement ($\sin(\gamma - \theta)$), which gave a quick response and was capable of providing both synchronisation and re-synchronisation effectively. The experimental responses were plotted for three phase fault and it was noted that, PLL will detect islanding within 0.0104 s and it can also switch to the

subsequent mode automatically. The PCC frequency variation was also within the prescribed limits as per IEEE standards (1%).

Acknowledgements

This work is supported by the Ministry of Power, Government of India through CPRI Bangalore, Karnataka under a project scheme (project code: RSOP/2015/DG 2/15122015, sanction date: 02/07/2016).

References

Basso, T. (2014) *IEEE 1547 and 2030 Standards for Distributed Energy Resources Interconnection and Interoperability with the Electricity Grid*, No. NREL/TP-5D00-63157, National Renewable Energy Lab.(NREL), Golden CO., USA.

Bei, T-Z. (2017) 'Accurate active islanding detection method for grid-tied inverters in distributed generation', *IET Renewable Power Generation*, Vol. 11, No. 13, pp.1633–1639.

Bifaretti, S. et al. (2015) 'Anti-islanding detector based on a robust PLL', *IEEE Transactions on Industry Applications*, Vol. 51, No. 1, pp.398–405.

Dong, D. et al. (2014) 'Modeling and design of islanding detection using phase-locked loops in three-phase grid-interface power converters', *IEEE Journal of Emerging and Selected Topics in Power Electronics*, Vol. 2, No. 4, pp.1032–1040.

Dou, C. et al. (2017) 'Improved droop control based on virtual impedance and virtual power source in low-voltage microgrid', *IET Generation, Transmission and Distribution*, Vol. 11, No. 4, pp.1046–1054.

Dragicevic, T. et al. (2017) 'Distributed and decentralized control architectures for converter-interfaced microgrids', *Chinese Journal of Electrical Engineering*, Vol. 3, No. 2, pp.41–52.

Gaonkar, D.N. (2010) 'Investigation on electromagnetic transients of distributed generation systems in the microgrid', *Electric Power Components and Systems*, Vol. 38, No. 13, pp.1486–1497.

Guerrero, J.M. et al. (2004) 'A wireless controller to enhance dynamic performance of parallel inverters in distributed generation systems', *IEEE Transactions on Power Electronics*, Vol. 19, No. 5, pp.1205–1213.

Guerrero, J.M. et al. (2005) 'Wireless-control strategy for parallel operation of distributed generation inverters', *Proceedings of the IEEE International Symposium on Industrial Electronics*, Vol. 2.

IEEE (2009) *IEEE Application Guide for IEEE Std 1547™ Photovoltaics, Dispersed Generation and Energy Storage*; *IEEE Standard for Interconnecting Distributed Resources with Electric Power Systems*.

Ketabi, A., Rajamand, S.S. and Shahidehpour, M. (2017) 'Power sharing in parallel inverters with different types of loads', *IET Generation, Transmission and Distribution*, Vol. 11, No. 10, pp.2438–2447.

Lin, C. et al. (2017) 'Decentralized reactive power optimization method for transmission and distribution networks accommodating large-scale DG integration', *IEEE Transactions on Sustainable Energy*, Vol. 8, No. 1, pp.363–373.

Luna, A. et al. (2015) 'Grid voltage synchronization for distributed generation systems under grid fault conditions', *IEEE Transactions on Industry Applications*, Vol. 51, No. 4, pp.3414–3425.

Pogaku, N. et al. (2007) Modeling, analysis and testing of autonomous operation of an inverter-based microgrid', *IEEE Transactions on Power Electronics*, Vol. 22, No. 2, pp.613–625

Pouresmaeil, E. et al. (2013) 'A control technique for integration of DG units to the electrical networks', *IEEE Transactions on Industrial Electronics*, Vol. 60, No. 7, pp.2881–2893.

Redfern, M.A., Usta, O. and Fielding, G. (1993) 'Protection against loss of utility grid supply for a dispersed storage and generation unit', *IEEE Transactions on Power Delivery*, Vol. 8, No. 3, pp.948–954.

Reznik, A. et al. (2014) 'LCL filter design and performance analysis for grid-interconnected systems', *IEEE Transactions on Industry Applications*, Vol. 50, No. 2, pp.1225–1232.

Rocabert, J., Luna, A., Blaabjerg, F. and Rodriguez, P. (2012) 'Control of power converters in AC microgrids', *IEEE Transactions on Power Electronics*, Vol. 27, No. 11, pp.4734–4749.

Sun, Y. et al. (2017) 'New perspectives on droop control in AC microgrid', *IEEE Transactions on Industrial Electronics*, Vol. 64, No. 7, pp.5741–5745.

Teodorescu, R. et al. (2004) 'Flexible control of small wind turbines with grid failure detection operating in stand-alone and grid-connected mode', *IEEE Transactions on Power Electronics*, Vol. 19, No. 5, pp.1323–1332.

Typhoon, H.I.L. (2016) *Inc. 'Typhoon Schematic Library User Guide'* [online] http://www.typhoon-hil. com.

Wang, X. et al. (2012) 'A review of power electronics based microgrids', *Journal of Power Electronics*, Vol. 12, No. 1, pp.181–192.

Wang, X. et al. (2015) 'Virtual-impedance-based control for voltage-source and current-source converters', *IEEE Transactions on Power Electronics*, Vol. 30, No. 12, pp.7019–7037.